An elastica robot: Tip-control in tendon-actuated elastic arms

Poornakanta Handral, Ramsharan Rangarajan *

Department of Mechanical Engineering, Indian Institute of Science, Bangalore, India

ARTICLE INFO

ABSTRACT

Various applications ranging from pipeline inspection to robot-assisted surgery require highly maneuverable devices with precisely controllable tips. In this article, we propose and experimentally validate a mechanics-based approach to manipulate the quasistatic planar motion of the tip of a flexible arm by controlling the tensions in a pair of cables attached to its centerline. We show that by adopting a geometrically nonlinear elastica model for the arm, by carefully accounting for configuration-dependent tendon loadings, and by interpreting the problem of manipulating the tip of the arm as one of load optimization, it is possible to realize a high degree of accuracy. In the process, we also identify interesting features of the tendon-loaded elastica problem. Our tip-control strategy is based solely on a predictive elastica model, does not require any sensors and does not employ any feedback. The resulting *elastica robot* is slender, remotely actuated, energy-efficient and miniaturizable.

1. Introduction

An emerging class of robots is composed of flexible structures and function by exploiting the compliances of their constitutive elements. Such robots are aimed at applications that demand high maneuverability for navigation in closed or cluttered environments, that require interaction with compliant substrates, and at applications where energy-efficiency is critical [1–4]. Their operating principle stands in stark contrast to traditional robots, which are typically composed of networks of links with actuated joints whose compliances are generally considered to be a hindrance for controlled operation [5,6].

Designing and fabricating flexible robots is a challenging endeavor, involving a multitude of considerations ranging from the choice of materials, power requirements, actuation mechanisms, sensors, multi-functionality, bulk manufacturability, and cost [7,8]. Material considerations are especially critical in soft robots made of biologically inspired and elastically soft materials such as gels and elastomers [9,10]. Our work here is motivated by the observation that developments in strategies for controlling flexible elements in robots lags behind technologies for designing and fabricating them [11].

In this context, we consider the problem of controlling the quasistatic planar motion of the tip of a flexible tendon-actuated elastic arm. Referring to the arrangement depicted in Fig. 1a consisting of a slender flexible arm clamped at one end and loaded by a pair of cables, we demonstrate that by modeling the highly deformable arm as an *elastica* and posing tip-control as a

problem of optimizing tensions in the cables, the tip of the arm can be accurately positioned within a feasible workspace. The resulting robot is energy-efficient since the strain energy stored in the arm during operation is fully recoverable, and is well suited for miniaturization.

A key factor that distinguishes various flexible robots is the actuation mechanism used. Tendon and pneumatic actuation are the most commonly used in practice [12–14]. Our choice of tendon actuation is based on its simplicity and ease of experimental realization. It additionally permits the actuators (motorized spools) to be located remotely. This is in contrast to designs where the actuating mechanism is an integral part of the deformable robotic arm. For instance, distributed pneumatic actuators that attempt to mimic muscular control are used in applications seeking to replicate bio-locomotion [15,16]. Similarly, incorporating actuatable fiber reinforcements in specific directions along an arm can help it achieve complex motions [17,18].

The tip-control problem for flexible arms that we consider here is certainly not new [19,20]. Early investigations modeled elastic arms as Euler–Bernoulli beams. Linearized kinematics is helpful in devising control algorithms [21] and is suitable for problems such as rest-to-rest maneuvers, but certainly not for our application where the arm necessarily undergoes large displacements and its sections undergo large rotations [22]. A pervasive assumption that attempts to account for finite deflections is the "constant curvature" approximation, wherein each section of the arm demarcated by tendon actuation points is assumed to bend into an arc of a circle [23]. The assumption is based on replacing tendon loads by point moments and has the convenient consequence of transforming the control problem into one of

(a) Tendon-actuated robotic arm.

(b) Idealization of the robotic arm as a tendon-loaded elastica.
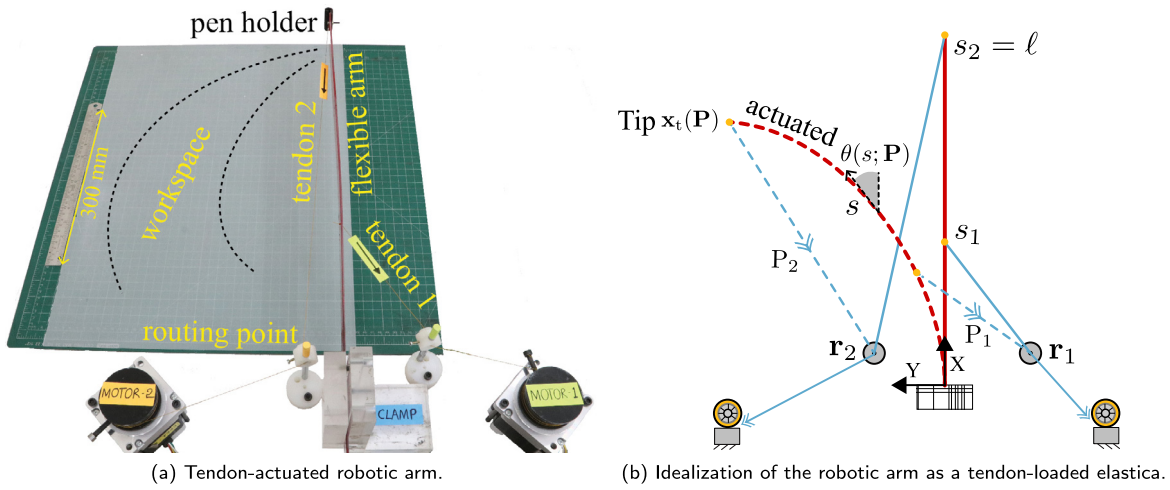
Fig. 1. Illustration of the experimental setup and its idealization. The polycarbonate arm in (a) has Young's modulus ≈ 2.2 GPa, length $\ell = 600$ mm, width 40 mm and thickness 3 mm, resulting in a bending stiffness of B ≈ 0.2 Nm^2. Each actuating tendon is attached to the centerline of the arm at one end and is routed through a fixed point to a motorized spool at the other. The first tendon is attached at a distance of $s_1 = 200$ mm from the clamped end while the second tendon is attached at $s_2 = 600$ mm to the tip of the arm. Routing points of the two tendons are located at $\mathbf{r}_1 = (46.3, -97.1)$ mm and $\mathbf{r}_2 = (26.1, 51.1)$ mm in the coordinate system indicated in (b). The cost of the setup, based on a conversion rate of INR 70/USD, is approximately \$255 and consists of $2 \times \$55$ for stepper motors, $2 \times \$50$ for motor drivers, and \$15 each for an Arduino board, DC power supply and materials.

inverse kinematics. We will show that such an approach is not suitable for our purposes, cf. [24]. Geometrically nonlinear models for flexible arms have been examined more recently, but are generally limited to the direct problem of predicting deflections when given the tensions in the cables [25]. Our approach to the tip placement problem is inspired by [26], and bears superficial similarities with certain inverse problems posed for the elastica to determine terminal forces and moments when given the locations of its end points [27].

2. An elastica model for tendon-actuated arms

The schematic in Fig. 1b represents an idealization of the setup in Fig. 1a. A straight elastic arm of length ℓ is loaded by a pair of tendons attached at distances $s = s_1$ and $s = s_2$ along its centerline, where $s \in [0, \ell]$ denotes the arc-length parameter of the centerline measured from the clamped end and $0 < s_1 < s_2 \leq \ell$. In the following, we set $s_2 = \ell$ and assume actuation using two tendons, but note that generalizations to multiple loads and to the case $s_2 < \ell$ are straightforward to work out. We presume the arm to be inextensible and its cross sections to be rigid and unshearable. Consequently, the deformation of the arm that results from imposing tensions $\mathbf{P} = (P_1, P_2)$ in the two tendons can be parameterized by the inclination angle $s \mapsto \theta(s; \mathbf{P})$ of the tangent to the centerline. In a Cartesian system centered at the clamped end and having its x-axis coincide with the undeformed beam, the tangent to the centerline is given by

$$\mathbf{t}(s; \mathbf{P}) = (\cos\theta(s; \mathbf{P}), \sin\theta(s; \mathbf{P})), \quad (1)$$

from where the coordinates of the deformed centerline follows as

$$s \mapsto \mathbf{x}(s; \mathbf{P}) = \int_{\xi=0}^{s} (\cos\theta(\xi; \mathbf{P}), \sin\theta(\xi; \mathbf{P})) \, d\xi. \quad (2)$$

In particular, $\mathbf{x}_1(\mathbf{P}) \triangleq \mathbf{x}(s_1; \mathbf{P})$ and $\mathbf{x}_2(\mathbf{P}) \triangleq \mathbf{x}(s_2; \mathbf{P})$ identify points of attachment of the tendons in the deformed configuration. The second argument $\mathbf{P}$ of θ, $\mathbf{t}$ and $\mathbf{x}$ explicitly denote their dependence on the loading. Though unnecessary for our current discussion, this dependence will be the basis for subsequent developments in Section 3.

To formulate the statement of moment balance governing static equilibrium of the arm, it is necessary to account for the fact

that the orientation of each tendon is configuration-dependent. Labeling the fixed routing points of the two cables by $\mathbf{r}_1$ and $\mathbf{r}_2$, the direction cosines of the cable orientations are given by

$$\mathbf{d}_i(\mathbf{P}) = \frac{\mathbf{r}_i - \mathbf{x}_i(\mathbf{P})}{\|\mathbf{r}_i - \mathbf{x}_i(\mathbf{P})\|}, \quad i = 1, 2, \quad (3)$$

and the actuating forces by

$$\mathbf{F}_i(\mathbf{P}) = P_i \, \mathbf{d}_i(\mathbf{P}) \text{ for } i = 1, 2. \text{ (no sum implied)} \quad (4)$$

Assuming a linear relationship between the curvature $\theta' \triangleq d\theta/ds$ of the centerline and the resultant moment, balancing internal and external moments at a point $0 < s < s_1$ yields

$$B\theta'(s; \mathbf{P}) = \sum_{i=1}^{2} (\mathbf{x}_i(\mathbf{P}) - \mathbf{x}(s; \mathbf{P})) \times \mathbf{F}_i(\mathbf{P}), \quad (5)$$

where B is the bending stiffness of the arm and $\times$ is the usual cross product operation on vectors. Differentiating Eq. (5) with respect to the parameter s, we get the statement of force balance:

$$B\theta''(s; \mathbf{P}) + \mathbf{t}(s; \mathbf{P}) \times (\mathbf{F}_1(\mathbf{P}) + \mathbf{F}_2(\mathbf{P})) = 0. \quad (6)$$

Arguing the same way, force balance at a point $s_1 \leq s < s_2$ is given by

$$B\theta''(s; \mathbf{P}) + \mathbf{t}(s; \mathbf{P}) \times \mathbf{F}_2(\mathbf{P}) = 0. \quad (7)$$

Eqs. (6) and (7) can be succinctly combined using the Heaviside function H as

$$B\theta''(s; \mathbf{P}) + \mathbf{t}(s; \mathbf{P}) \times (H(s_1 - s)\mathbf{F}_1(\mathbf{P}) + \mathbf{F}_2(\mathbf{P})) = 0, \quad (8)$$

which is supplemented with boundary conditions $\theta(0; \mathbf{P}) = 0$ and $\theta'(\ell; \mathbf{P}) = 0$ representing the clamped and moment-free ends. Eq. (8) is our model for the tendon-actuated arm − it determines the deflection of the arm when given the tensions in each cable.

Eq. (8) is equivalent to the principle of virtual work

$$\begin{aligned} G(\theta, \delta\theta) \triangleq &\int_{s=0}^{\ell} B\theta' \delta\theta' \, ds \\ &- \int_{s=0}^{s_1} (\mathbf{t}(s; \mathbf{P}) \times \mathbf{F}_1(\mathbf{P})) \, \delta\theta \, ds \\ &- \int_{s=0}^{s_2} (\mathbf{t}(s; \mathbf{P}) \times \mathbf{F}_2(\mathbf{P})) \, \delta\theta \, ds = 0, \end{aligned} \quad (9)$$

which holds for all admissible variations $s \mapsto \delta\theta(s)$. The form of Eq. (9) is directly useful for computing θ using a finite element method. We employ a straightforward implementation to this end, comprising of piecewise linear elements to discretize the inclinations $s \mapsto \theta(s; \mathbf{P})$, consistent linearization of G to determine the stiffness matrix, and a Newton–Raphson scheme for resolving the resulting set of nonlinear algebraic equations. We refer to [26, Section 2] for comparisons of numerical solutions of Eq. (9) with closed-form solutions derived for special cases in [28,29] and with experimental measurements.

Nonlinearity in the model represented by Eq. (8) is purely geometrical and stems from three sources — computing curvatures of the centerline exactly, measuring moment arms of loads without approximation, and accounting for the dependence of tendon inclinations on the deformation. Implicit in the linear assumption between curvatures and resultant moments is the requirement that strains be small and that the material remain elastic. Hence, the model in Eq. (8) permits large rotations and displacements, but is necessarily restricted to small curvatures.

3. Tip-control through load optimization

We now proceed to the problem of placing the tip of the flexible arm in Fig. 1 at a desired location $\mathbf{x}_d$ by imposing suitable tensions in the cables. To this end, introduce a cost function

$$E(\mathbf{P}) \triangleq \frac{1}{2} \|\mathbf{x}_d - \mathbf{x}_t(\mathbf{P})\|^2 \qquad (10)$$

to measure the deviation of the tip location $\mathbf{x}_t(\mathbf{P}) \triangleq \mathbf{x}(\ell; \mathbf{P})$ of the arm at static equilibrium, from the desired position $\mathbf{x}_d$. The dependence of E on cable tensions in Eq. (10) is implicitly conveyed by the tip location computed using Eq. (2). We now pose tip-control as a parameter optimization problem for P_1 and P_2:

$$\text{Find } \mathbf{P} \in \underset{\mathbf{P} \in [\mathbb{R}_{\geq 0}]^2}{\arg\min} \{E(\mathbf{P}) : G(\theta, \delta\theta) = 0 \ \forall \delta\theta\}. \qquad (11)$$

Eq. (11) is a minimization problem that is constrained by the nonlinear state equation (8) and the convex constraints $P_{1,2} \geq 0$ on the set of feasible solutions.

If the target point $\mathbf{x}_d$ lies within the workspace (see Eq. (18)), the non-negative function E necessarily attains its global minimum value of zero for at least one pair of cable tensions. For such points, we identify the minimizer in Eq. (11) by resorting to a numerical gradient descent scheme. For this purpose, we compute the gradient of E next.

Differentiating Eq. (10) with respect to the tension P_i, we get

$$\frac{\partial E}{\partial P_i} = (\mathbf{x}_t(\mathbf{P}) - \mathbf{x}_d) \cdot \frac{\partial \mathbf{x}_t(\mathbf{P})}{\partial P_i}, \quad i = 1, 2. \qquad (12)$$

In Eq. (12), $\partial \mathbf{x}_t(\mathbf{P})/\partial P_i$ represents the *sensitivity* of the tip of the arm to the tension in the ith cable, and is computed using Eq. (2) as

$$\frac{\partial \mathbf{x}_t(\mathbf{P})}{\partial P_i} = \frac{\partial}{\partial P_i} \int_{s=0}^{\ell} (\cos\theta(s; \mathbf{P}), \sin\theta(s; \mathbf{P})) \, ds$$

$$= \int_{s=0}^{\ell} \underbrace{(-\sin\theta(s; \mathbf{P}), \cos\theta(s; \mathbf{P}))}_{\mathbf{n}(s;\mathbf{P})} \underbrace{\frac{\partial\theta(s; \mathbf{P})}{\partial P_i}}_{\alpha_i(s;\mathbf{P})} \, ds$$

$$= \int_{s=0}^{\ell} \mathbf{n}(s; \mathbf{P}) \alpha_i(s; \mathbf{P}) \, ds, \qquad (13)$$

where $\mathbf{n}$ is the normal to the centerline and α_i is the sensitivity of the solution θ to the load P_i. Evidently, if we can compute $s \mapsto (\alpha_1(s; \mathbf{P}), \alpha_2(s; \mathbf{P}))$, we can compute the sensitivity of the tip location $\mathbf{x}_t(\mathbf{P})$ to each load using Eq. (13), then the gradient

of E using Eq. (12), and therefore identify a descent direction for minimizing E. To this end, differentiating Eq. (8) with respect to P_i, we get

$$B\alpha_i''(s; \mathbf{P}) + \frac{\partial\mathbf{t}(s; \mathbf{P})}{\partial P_i} \times (H(s_1 - s)\mathbf{F}_1(\mathbf{P}) + \mathbf{F}_2(\mathbf{P}))$$

$$+ \mathbf{t}(s; \mathbf{P}) \times \left(H(s_1 - s)\frac{\partial\mathbf{F}_1(\mathbf{P})}{\partial P_i} + \frac{\partial\mathbf{F}_2(\mathbf{P})}{\partial P_i} \right) = 0, \qquad (14)$$

which, along with the boundary conditions $\alpha_i(0; \mathbf{P}) = 0$ and $\alpha_i'(\ell; \mathbf{P}) = 0$ that follow from those for θ, defines a boundary value problem for the sensitivities $s \mapsto (\alpha_1(s; \mathbf{P}), \alpha_2(s; \mathbf{P}))$.

Sensitivities of $\mathbf{t}$, $\mathbf{F}_1$ and $\mathbf{F}_2$ appearing in Eq. (14) can be explicitly computed using their definitions in Eqs. (1), (3) and (4). For the tangent, we have

$$\frac{\partial\mathbf{t}(s; \mathbf{P})}{\partial P_i} = (-\sin\theta(s; \mathbf{P}), \cos\theta(s; \mathbf{P}))\alpha_i(s; \mathbf{P})$$

$$= \mathbf{n}(s; \mathbf{P})\alpha_i(s; \mathbf{P}). \qquad (15)$$

Sensitivities of the actuating forces follow from Eqs. (3) and (4) as

$$\frac{\partial\mathbf{F}_j(\mathbf{P})}{\partial P_i} = \delta_{ij}\mathbf{d}_j(\mathbf{P}) + P_j\frac{\partial\mathbf{d}_j(\mathbf{P})}{\partial P_i} \qquad (16)$$

where δ_{ij} is the Kronecker-delta symbol and

$$\frac{\partial\mathbf{d}_j(\mathbf{P})}{\partial P_i} = \frac{\partial}{\partial P_i} \left(\frac{\mathbf{r}_j - \mathbf{x}_j(\mathbf{P})}{\|\mathbf{r}_j - \mathbf{x}_j(\mathbf{P})\|} \right)$$

$$= \left(\frac{\mathbf{d}_j(\mathbf{P}) \otimes \mathbf{d}_j(\mathbf{P}) - \mathbf{I}}{\|\mathbf{r}_j - \mathbf{x}_j(\mathbf{P})\|} \right) \frac{\partial\mathbf{x}_j(\mathbf{P})}{\partial P_i}, \qquad (17)$$

where $\otimes$ is the dyadic product.

Algorithm 1 summarizes the load optimization scheme for tip-control in a stepwise manner. In our implementation of the algorithm, we use the sparse data structures and nonlinear solvers provided by the PETSc library, and the gradient descent routines with adaptive step sizing implemented in the TAO optimization library [30]. Fig. 2 uses an example to illustrate the descent iterations in the algorithm to place the tip of the arm in Fig. 1 at a specified location. Since the trivial initial guess $\mathbf{P} = (0, 0)$ for cable tensions is far from the optimal value, the algorithm requires over a dozen iterations to converge. As depicted in Fig. 2b, some of the intermediate load iterates are even inadmissible since the constraints $P_{1,2} \geq 0$ were not explicitly enforced. The monotonic decrease in the cost function observed in Fig. 2c is a direct consequence of accurately computing its sensitivities in Eq. (12). The tolerance set for convergence of E implies an accuracy of 10^{-5} mm for the tip position.

A few additional remarks are in order. Geometric nonlinearities inherent in the model for the direct problem are evident in the sensitivity calculations as well. Eq. (15) measures the influence of cable tensions on the local curvature. Eq. (17) reveals how the tension in each cable influences the orientations of every cable, and hence, an innate coupling between the actuating forces. Despite the seemingly tedious nature of Eq. (14) that results from substituting the expressions in Eqs. (15) to (17), Eq. (14) is in fact a linear ordinary differential equation for α_i, $i = 1, 2$. Hence, we approximate α_1 and α_2 using a linear finite element method and exploit the fact that the stiffness matrices required to compute the two sensitivities are identical. The weak forms required for these calculations can be derived either from Eq. (14), or by differentiating Eq. (9) with respect to P_1 and P_2.

4. Experimental realization

We devote this section to experimentally examining the accuracy of tip-control realizable with Algorithm 1. Fig. 1a shows
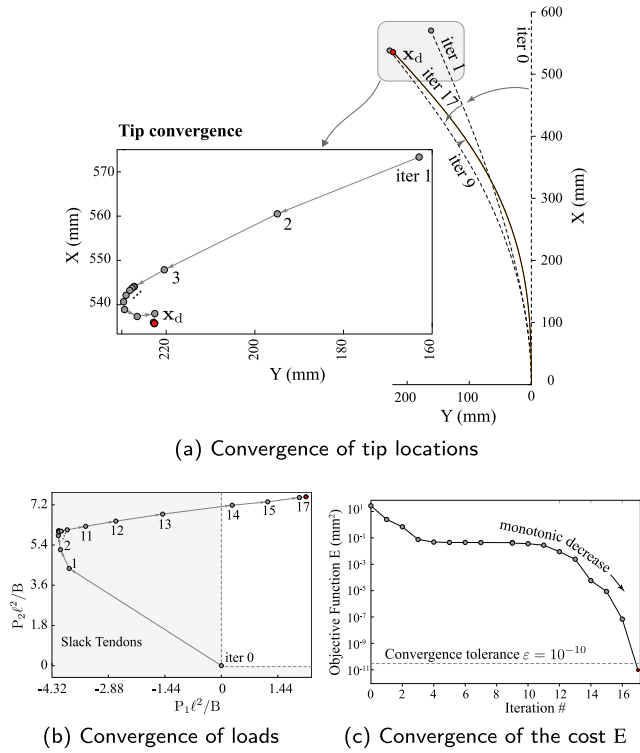
(a) Convergence of tip locations

(b) Convergence of loads   (c) Convergence of the cost E

Fig. 2. An example illustrating the iterations in Algorithm 1 to compute the optimal cable tensions to place the tip of the arm in Fig. 1 at $\mathbf{x}_d = (535.8, 222.6)\,\text{mm}$.

Algorithm 1 Gradient descent for load optimization

1: **function** TIPCONTROL($\mathbf{P}^0, \mathbf{x}_d, \gamma, \varepsilon$)
2:     $\mathbf{x}_d \leftarrow$ target tip position
3:     $\mathbf{P} \leftarrow \mathbf{P}^0$: initial guess for loads
4:     $\gamma \leftarrow$ descent step size
5:     $\varepsilon \leftarrow$ tolerance for convergence of E
6:     **while** true **do**
7:        Compute θ satisfying $G(\theta, \delta\theta) = 0 \; \forall \, \delta\theta$
                                 ▷ See Eq. (9)
8:        **if** $E(\mathbf{P}) < \varepsilon$ **then**
9:           break!   ▷ Tip location has converged
10:       **end if**
11:       Compute (α_1, α_2) satisfying Eq. (14)
12:       Compute $\nabla_{\mathbf{P}} E(\mathbf{P})$ using Eq. (12)
13:       Update load guesses $\mathbf{P} \leftarrow \mathbf{P} - \gamma \, \nabla_{\mathbf{P}} E(\mathbf{P})$
14:     **end while**
15:     Compute tendon lengths

$$L_i = \|\mathbf{x}_i(\mathbf{P}) - \mathbf{r}_i\|, \; i = 1, 2.$$

16:       **return** Tensions $\mathbf{P}$ and tendon lengths (L_1, L_2)
17: **end function**

---

details of the experimental setup used. Physical properties of the arm and geometric dimensions relevant to the setup are mentioned in the caption under the figure. Small holes located along the centerline of the arm serve as attachment points for two metal-reinforced cables. The cables are sufficiently stiff ($\approx 4.9\,\text{kN/mm}$), which warrants treating them as rigid structures when in tension. The length of the arm is short enough so that its centerline does not visibly sag due to gravity, and its width is large enough to reduce axial twisting caused by small deviations

between the plane of the centerline and the planes swept by the tendons. Each cable is routed through a fixed point to a motorized spool, which reels in/out the cable, thereby controlling its length and in turn the tension it bears. A light attachment holds a pen to trace the location of the tip as the arm deforms.

4.1. Length controlled experiments

It is possible to impose the tensions (P_1, P_2) computed by Algorithm 1 by coupling each cable with a tension gauge. For the sake of simplicity and to avoid errors caused by friction between cables and their routing posts, we instead impose the cable lengths (L_1, L_2) computed in the algorithm. Hence, actuating the arm translates to prescribing the number of revolutions required of each motor. Equivalence between load and length control requires a monotonic relationship between cable lengths and tensions during operation, which we have verified to be the case in our examples.

4.2. Examples

We use the two examples in Fig. 3 to examine the accuracy of tip-control realizable using Algorithm 1. Movies of these experiments are provided as supplementary materials accompanying this article. For the example in Fig. 3a, Algorithm 1 precomputes the cable lengths required to place the tip of the arm along the edges of an equilateral triangle, along its incircle and along its circumcircle. Dashed arrows in the figure indicate the sequence in which points are provided to the algorithm. Imposing the computed cable lengths by slowly operating the two motors causes the pen attached at the tip of the arm to trace the prescribed shapes. The figure shows a scan of the drawing sheet from the experiment and snapshots of the arm during the tracing process. The dimensions superimposed on the traced shapes demonstrate that edge lengths of the triangle, radii of the two circles, angles between the triangle edges, and tangency of the incircle to the edges are all nearly exact. Three repetitions of the experiment revealed errors in lengths and angles to be consistently under 2 mm and 1°, respectively.

In the second example in Fig. 3b, the sequence of points provided to Algorithm 1 are shown as green dots superimposed on the drawing sheet from the experiment. Actuating the arm by imposing the sequence of computed cable lengths results in the tip tracing the curve in orange, which closely follows the specified set of points. The figure also shows snapshots of the arm as it traces a convoluted curve. Small deviations not exceeding 2 mm are visible at a few locations.

4.3. Workspace

An important consideration in robotics applications is the extent of the workspace. In our context, the workspace is the locus of the tip of the arm as the tensions in the cables are varied:

$$\mathcal{W}_0 \triangleq \{\mathbf{x}_t(\mathbf{P}) \, : \, P_{1,2} \geq 0\}. \tag{18}$$

Besides showing that $\mathcal{W}_0$ is a set parameterized by P_1 and P_2, the implicit dependence of the map $\mathbf{P} \mapsto \mathbf{x}_t(\mathbf{P})$ on the design specifications, namely, the length of the arm, the number of loading tendons used, the locations of tendon attachments along the arm, and the routing point set for each tendon, reveals that $\mathcal{W}_0$ is determined by these parameters. The set of green points in Fig. 4 is a sampling $\mathcal{W}_0^{\text{sam}}$ of $\mathcal{W}_0$ computed using Algorithm 1. The figure shows, as expected, that the workspace is bounded on one side by the locus of the tip realized by setting $P_1 = 0$. Regions in the half-plane $y \geq 0$ that are not sampled well owing to numerical convergence difficulties are indicated in the figure. To adhere closely
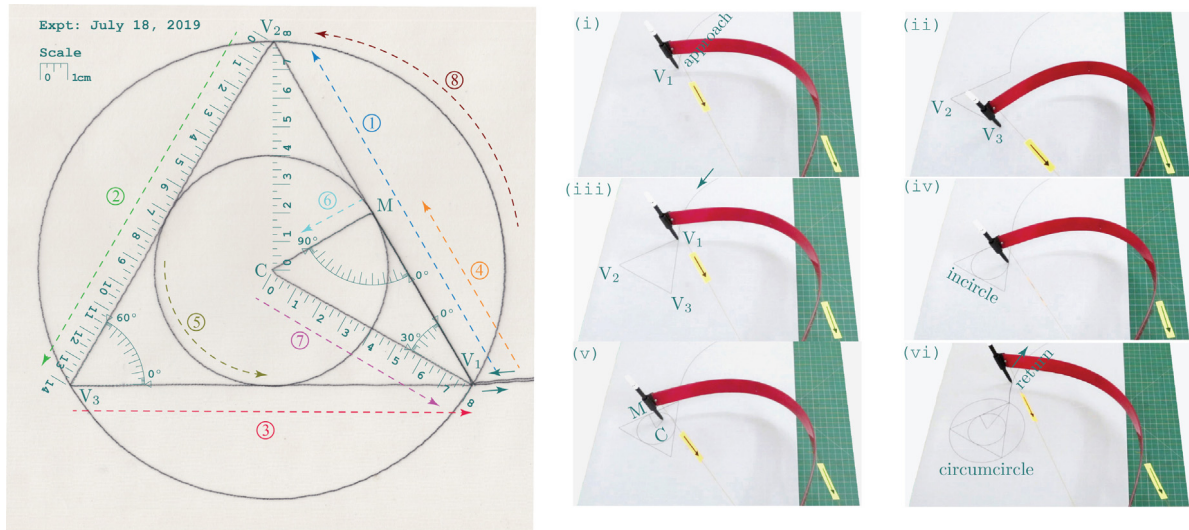
(a) The image on the left shows the drawing sheet from an experiment in which the tip of the arm traces an equilateral triangle of side $80\sqrt{3} \approx 138.56$ mm, its incircle (radius 40 mm) and its circumcircle (radius 80 mm). Arrows in the image indicate the sequence in which the different shapes are traced. The example contains a number of geometric parameters that help to examine accuracy— lengths of the triangle edges, the angles between them, radii of the circles, their concentricity, tangency of the incircle to the triangle edges and proximity of the triangle vertices to the circumcircle. Superimposed measurements reveal the accuracies of various dimensions. Snapshots taken during the tracing process are shown on the right.
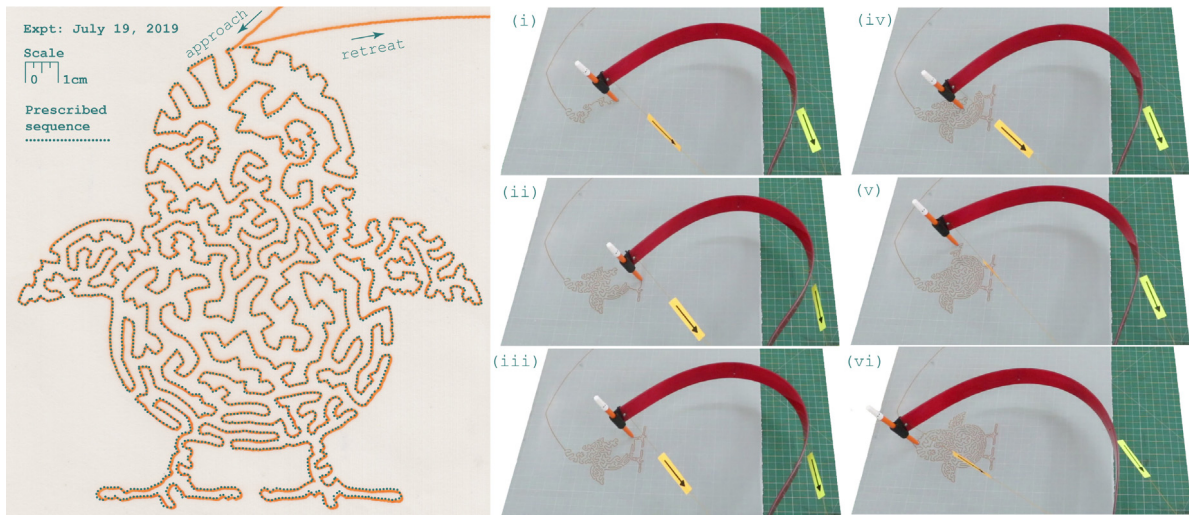
(b) A second example shows the drawing sheet from an experiment in which the tip of the arm traces the convoluted (yet connected) curve in orange by imposing the cable lengths computed by Algorithm 1 for the given sequence of points indicated by green dots. As observed in (a), deviations from target locations remain small (< 2 mm). In fact, any large deviations would have manifested as self-intersections in the traced curve. Snapshots from the experiment are shown on the right.

Fig. 3. Experiments demonstrating tip-control using Algorithm 1. Videos of the experiments are provided as supplementary materials.

to our experimental investigations, we limit the sampling of the workspace to just the upper half plane. Hence, $\mathcal{W}_0^{\text{sam}}$ only samples a subset of $\mathcal{W}_0$. The figure also shows a circular path that represents the workspace of a rigid link of length ℓ hinged at the origin.

Besides non negativity of loads, additional constraints restrict the workspace in practice.

(i) To facilitate repeated use, it is necessary to ensure that the material constituting the arm does not yield or fracture. Without loss of generality, such a restriction can be represented as an upper bound on the maximum strain permitted during deformation. Correspondingly, the locus of the tip is limited to the set

$$\mathcal{W}_Y \triangleq \mathcal{W}_0 \cap \{\mathbf{x}_t(\mathbf{P}) : \max_{0 \le s \le \ell} |\theta'(s; \mathbf{P})| < 2\varepsilon_Y/h\}, \tag{19}$$

where ε_Y is the failure strain and h is the thickness of the arm.

(ii) The next restriction stems from the requirement that the workspace only consist of tip locations of configurations at stable equilibrium. We denote the corresponding set by

$$\mathcal{W}_S \triangleq \mathcal{W}_0 \cap \{\mathbf{x}_t(\mathbf{P}) : \theta(s; \mathbf{P}) \text{ is stable}\}. \tag{20}$$

It is important to note that stability of equilibria in load and length controlled settings are quite different, see Section 4.6. For the purpose of discussing the extent of the workspace, we assume a load controlled scenario.

(iii) Depending on the application, the total energy available for operating the arm may be limited. This is the case, for instance, when the energy source is a battery pack. Neglecting frictional losses, the strain energy stored in the arm is a direct measure of the total energy required. Energy considerations hence limit the
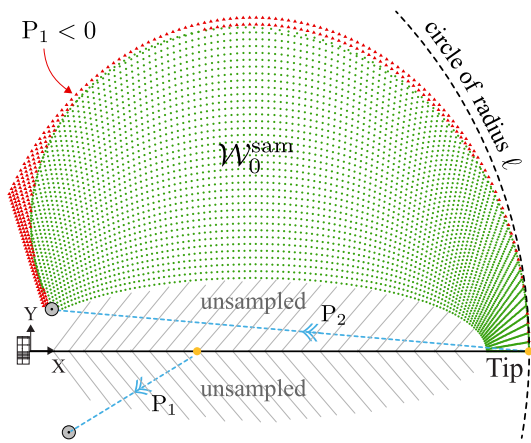
Fig. 4. The set $\mathcal{W}_0^{\mathrm{sam}}$ consisting of 4201 green points, is a sampling of the workspace $\mathcal{W}_0$ of the elastic arm in the half plane $y \geq 0$. Red points bounding $\mathcal{W}_0^{\mathrm{sam}}$ on one side require $P_1 < 0$ and are therefore not part of the workspace. The dashed line in black represents the locus of the tip of a rigid link of length ℓ hinged at the origin.

workspace to

$$\mathcal{W}_{\mathrm{E}} \triangleq \mathcal{W}_0 \cap \{\mathbf{x}_{\mathrm{t}}(\mathbf{P}) \,:\, \frac{1}{2}\int_{s=0}^{\ell} \mathrm{B}\theta'^2(s;\mathbf{P})\,ds < \mathrm{SE}_{\max}\}. \quad (21)$$

(iv) Closely related to Eq. (21), and particularly relevant to our setup, are limitations on the workspace arising from the torque ratings of the motors driving the tendon spools. Assuming the capacities of the two motors to be identical and converting their ratings to a critical force P_{crit}, the workspace is limited to

$$\mathcal{W}_{\mathrm{P}} \triangleq \mathcal{W}_0 \cap \{\mathbf{x}_{\mathrm{t}}(\mathbf{P}) \,:\, P_{1,2} < P_{\mathrm{crit}}\}. \quad (22)$$

Fig. 5 examines each of the above four criteria over the set of sample points $\mathcal{W}_0^{\mathrm{sam}}$. The examples discussed in Section 4.2 are superimposed in the images to help examine the ranges of parameters realized in the experiments. Fig. 5a shows contours of the non dimensionalized maximum curvature $\ell\kappa_{\max}(\mathbf{P}) = \max_{0 \leq s \leq \ell} |\ell\theta'(s;\mathbf{P})|$. Setting the strain to failure by yielding as $\varepsilon_{\mathrm{Y}} = 2.5\%$ for polycarbonate and noting that the thickness of the arm is h = 3 mm, the maximum permissible curvature according to Eq. (19) is $(2 \times 0.025/3)\,\mathrm{mm}^{-1}$, which when non dimensionalized by ℓ, sets a limiting value of 10. The figure shows that the normalized maximum curvatures at points sampled in our experiments do not exceed 6.5. Hence, the arm operates safely within the bounds set by material failure considerations.

Next, we examine the restriction on the workspace imposed by stability considerations in Eq. (20). Since tendon loadings are non conservative, energy-based stability criteria do not apply. We adopt a linearized dynamics stability criterion instead [31]. While this usually requires resolving a generalized eigenvalue problem involving the mass and stiffness matrices, a simplification is possible in our case. We exploit the fact that the finite element mesh used is uniform and employ nodal mass lumping, so that the mass matrix is reduced to a multiple of the identity.[1] Hence the spectrum of the finite element stiffness matrix $\mathbf{K}(\mathbf{P})$ is a direct indicator of stability. In particular, a set of real-valued positive eigenvalues implies stability. Fig. 5b shows contours of the smallest eigenvalue $\lambda_{\min}(\mathbf{K}(\mathbf{P}))$ of $\mathbf{K}(\mathbf{P})$ at each sample point in $\mathcal{W}_0^{\mathrm{sam}}$ normalized by the factor B/ℓ. The stiffness matrix $\mathbf{K}(\mathbf{P})$ is determined by consistently linearizing Eq. (9) and is in general

non symmetric. We use the SLEPc library [32] to compute its spectrum. The smallest normalized value realized over all sample points is $\approx 1.8 \times 10^{-3}$. The sensitivities $\alpha_{1,2}(s;\mathbf{P}) = \partial\theta(s;\mathbf{P})/\partial P_{1,2}$ provide an alternate way of inferring the absence of snap-through instabilities, because they become unbounded at critical loads [33,34]. Both α_1 and α_2 remain bounded at all sample points in $\mathcal{W}_0^{\mathrm{sam}}$.

Fig. 5c shows contours of the strain energy normalized by the factor $\mathrm{SE}_0 = B/2\ell \approx (1/6)\,\mathrm{J}$. We find that points sampled in the experiments in Fig. 3 are bounded by the contour line of value 18, implying that the energy required at any instant during these experiments do not exceed 3 J. A small amount of additional energy is required to overcome frictional losses at the tip of the tracing pen. Fig. 5d shows level sets of the two tendon loads normalized by the factor B/ℓ^2. As expected, the first cable attached closer to the clamped end requires higher actuation forces than the second cable attached to the tip. We observe from the figure that the maximum force required during the experiments does not exceed $40\,B/\ell^2 \approx 22.2\,\mathrm{N}$. The torque ratings of the motors used in our experiments are 35 kg-cm and each tendon spool has a radius of 3.1 cm, resulting in a critical load of $P_{\mathrm{crit}} \approx 112.9\,\mathrm{N}$. The tensions realized in the experiments are hence much smaller than the critical capacities of the motors.

We conclude this discussion with a remark on the influence of the material constitution of the arm on the extent of the workspace. Criteria (21) and (22) involve the bending stiffness, and hence the Young's modulus of the material. Criterion (19) introduces an independent material property, namely, the strain (or stress) to failure. As a thought experiment, consider replacing the material of the arm with a metal, say Aluminum, while retaining all geometric dimensions unchanged. Note that the non dimensionalized curvature strains, energies and tendon loads plotted in Fig. 5 remain unchanged as well. The bending stiffness of the metallic arm is larger by a factor of about 30 while the strain to failure is smaller by a factor of about 10. Then, following simple calculations analogous to the ones discussed above, we find that the metallic arm would have in fact yielded and the critical motor load exceeded during the course of performing the experiments in Fig. 3.

4.4. Non intuitive operation

With possible application to precision surgical procedures in mind, it is appealing to consider controlling the tendons operating the elastica robot by hand instead of using motors. By leveraging complex haptic and visual feedback, it may be possible to effectively *learn* what Algorithm 1 accomplishes. Based on our experience, however, this turns out to be a very challenging task. We use the example in Fig. 3a to elucidate why.

Fig. 6a shows the tensions and cable lengths computed by Algorithm 1 to trace each segment in Fig. 3a. We find that even tracing straight segments requires nonlinear variations in cable tensions and lengths. The large disparities in tensions required in the two cables is also apparent, reflecting the differences in the compliances of the arm at the points of actuation. Furthermore, as indicated in Fig. 6b, the cables undergo significant orientation changes during operation.

Fig. 6b additionally examines the sensitivity of the tip to the tensions in the cables as it traces the specified shape. The blue and orange arrows in the figure are scaled representations of the vectors $\partial\mathbf{x}_{\mathrm{t}}/\partial P_1$ and $\partial\mathbf{x}_{\mathrm{t}}/\partial P_2$, respectively, computed using Eq. (13). These vectors indicate how the tip responds to small changes in cable tensions. The polar plot included in the figure reveals that both magnitudes and orientations of tip sensitivities change appreciably with tip location. The plot also shows that the tip is roughly ten times more sensitive to the second cable than
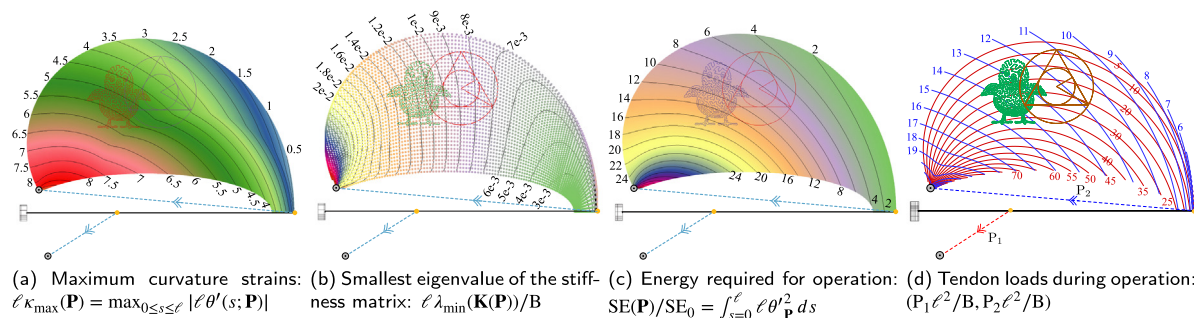
---

[1] This simplification incurs a small error by doubling the nodal mass at the tip of the arm. This can be crudely justified as a way of accounting for the pen holder attached to the tip.

(a) Maximum curvature strains: $\ell\kappa_{\max}(\mathbf{P}) = \max_{0 \le s \le \ell} |\ell\theta'(s;\mathbf{P})|$

(b) Smallest eigenvalue of the stiffness matrix: $\ell\lambda_{\min}(\mathbf{K}(\mathbf{P}))/\mathrm{B}$

(c) Energy required for operation: $\mathrm{SE}(\mathbf{P})/\mathrm{SE}_0 = \int_{s=0}^{\ell} \ell\theta'^2_{\mathbf{P}} \, ds$

(d) Tendon loads during operation: $(\mathrm{P}_1\ell^2/\mathrm{B}, \mathrm{P}_2\ell^2/\mathrm{B})$

Fig. 5. Examining restrictions on the workspace based on strain, stability, energy and load considerations. Figures (a)–(d) show contours of non dimensionalized variables over the sampling $\mathcal{W}_0^{\text{sam}}$ of the workspace depicted in Fig. 4. The shapes traced during the experiments in Fig. 3 are superimposed in each plot.
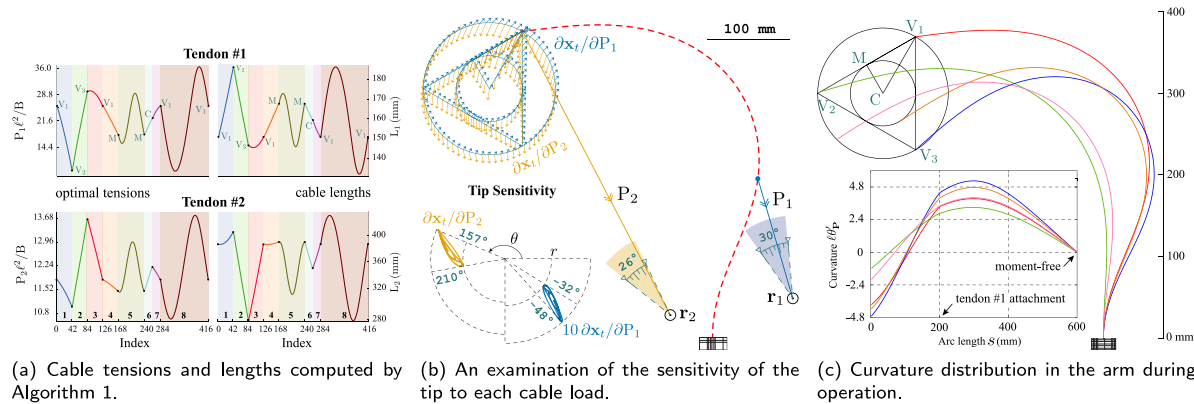

(a) Cable tensions and lengths computed by Algorithm 1.

(b) An examination of the sensitivity of the tip to each cable load.

(c) Curvature distribution in the arm during operation.

Fig. 6. Referring to the example in Fig. 3a, (a) shows the non trivial variations in cable tensions and length required for tracing each section. Figure (b) illustrates the sensitivity of the tip to the tension in each cable. Examining the curvature distribution in the arm in (c) categorically refutes the constant curvature assumption that is commonly invoked in the literature.

it is to the first, again, reflecting the compliances at the points of attachment of the two cables. In summary, the tip response to cable tensions is highly configuration dependent, which makes controlling it very non intuitive. This observation also explains why Algorithm 1 cannot simply be replaced by a brute force search for optimal cable tensions.

4.5. Observations

(i) We restrict the actuation in our examples to two tendons because it is the minimum number required for the workspace to have a finite area measure. Using additional tendons will likely increase the extent of the workspace.

(ii) Values of the parameters $s_{1,2}$ and $\mathbf{r}_{1,2}$ that define the details of tendon loadings in the experimental setup are not particularly special. Rather, they are chosen so that the arm is loaded along independent directions by the two tendons. Level sets of the two tendon loads shown in Fig. 5d demonstrate this point. For the sake of brevity, we have not included experiments such as those in Fig. 3 performed with alternate values of these parameters.

(iii) A useful consequence of controlling lengths in the experiments is that it suffices to compute the ratios $\mathrm{P}_1\ell^2/\mathrm{B}$ and $\mathrm{P}_2\ell^2/\mathrm{B}$ in Algorithm 1. Hence, we completely bypass the need to determine the bending stiffness of the arm.

(iv) Although Algorithm 1 controls the operation of the arm, the examples in Fig. 3 in fact mainly serve to validate the model for the direct problem in Eq. (8). This is because, by providing target points that lie within the workspace and by using a tolerance $\varepsilon = 10^{-10}$ mm^2 for detecting convergence of E, we ensure that the tensions computed by Algorithm 1 position the tip within 10^{-5} mm of the desired location. Hence, the load optimization algorithm does not introduce any meaningful error in the tip

position. Small deviations observed in the examples are instead the cumulative result of errors in experiments and of assumptions in the model for the direct problem.

(v) Good initial guesses for cable tensions in Algorithm 1 are essential to ensure its convergence and to limit the number of descent iterations required. In the examples in Fig. 3, we use the tensions computed for a target point as the initial guess to position the tip at the next location. With this approach, each invocation of the algorithm typically requires fewer than 5 iterations to converge. Executing a serialized implementation of the algorithm on a desktop computer requires less than a second per target point when using 180 elements to discretize the arm.

(vi) Since our model does not account for the inertia of the arm, the experiments in Fig. 3 were performed sufficiently slowly. With the motors operating at approximately 13 s/rev, Fig. 3a took approximately 3 min to trace, while the curve in Fig. 3b took about 9 min. These times correspond to tracing speeds of about 7.5 mm/s and 5.6 mm/s, respectively, for the two experiments. At these low speeds, friction at the pen tip effectively damps out small vibrations of the arm. We arrived at these tracing speeds by trial and error. A more systematic procedure follows from using eigenfrequencies to set upper bounds for tracing speeds. Furthermore, since these frequencies are configuration dependent, computing them can help to tune tracing speeds in an adaptive manner.

(vii) The weight of the arm, the initial tension in the cables (just taut condition) and friction between the pen tip and the drawing sheet are important sources of error in our experiments that are neither modeled nor measured. To reduce errors due to friction, we allow the pen to slide freely within its holder so that the normal force exerted by the pen on the sheet remains small and approximately equal to the weight of the pen.
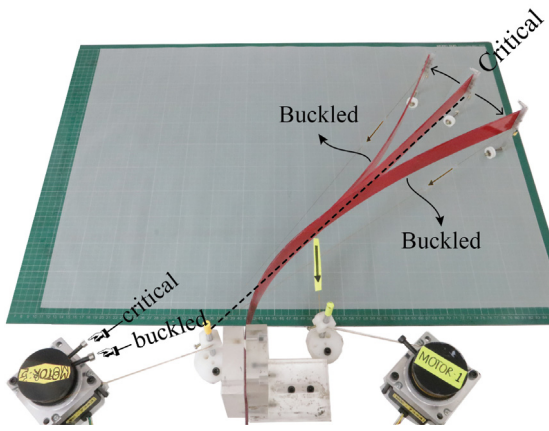
Fig. 7. A stroboscopic image showing a buckling instability in the tendon-driven elastic arm. At the critical state, the first tendon loads the arm while the second is just taut. The straight section of the arm between the two attachment points is aligned with the orientation of the second tendon. Engaging the second tendon causes the straight section to buckle like an Euler column.

(viii) The geometric nature of the tip-control problem is made conspicuous by the special case in which both tendons are attached to the tip of the arm, i.e., the case $s_1 = s_2$. Then, the optimal cable lengths (L_1, L_2) required to position the tip at $\mathbf{x}_d$ can be computed as the radii of a pair of circles centered at the routing points $\mathbf{r}_1$ and $\mathbf{r}_2$ and intersecting at $\mathbf{x}_d$.

### 4.6. Load and length controlled systems

The interesting scenario, wherein calculations underlying Algorithm 1 are load controlled, while their experimental realizations are length controlled, can be interpreted as an opportunistic transformation of variables. To wit, formulating the equilibrium equations in terms of cable lengths, though possible, is tedious. In the same vein, cable lengths, rather than tensions, are easier to control in our experiments.

Though convenient, this approach is not without caveats. Notably, it is not straightforward to relate instabilities possible in the load and length controlled settings. Our load controlled numerical simulations reveal the existence of numerous snap through instabilities when the tip of the arm is located in the half-plane $y < 0$. However, these are generally not realizable in length controlled experiments, presumably due to the one-sided kinematic constraints

$$\|\mathbf{x}_i - \mathbf{r}_i\| \leq \ell_i \quad \text{for } i = 1, 2, \tag{23}$$

imposed by the inextensibilities of the two tendons. In particular, admissible perturbations in the length controlled setting are required to satisfy Eq. (23), while those in the load controlled setting do not. Nevertheless, instabilities are possible with length control as well— Fig. 7 shows an example of a buckling instability. At the critical state, the first tendon loads the arm and the second tendon is just taut. The section of the arm between the two attachment points $\mathbf{x}_1$ and $\mathbf{x}_2$ is nominally straight, and crucially, aligned with the orientation of the second tendon. Engaging the second tendon, by reducing its length by a few millimeters while leaving the length of the first tendon unchanged, compresses the straight section of the arm like an Euler column and causes it to buckle to one of two states.

Distinctions between load and length controlled deformations also manifest when examining solution multiplicity. Fig. 8 shows three equilibrium configurations labeled as states 1, 2 and 3. States 1 and 2 have identical cable lengths $(L_1, L_2) = (147.1, 472.5)$ mm, while states 1 and 3 have identical cable
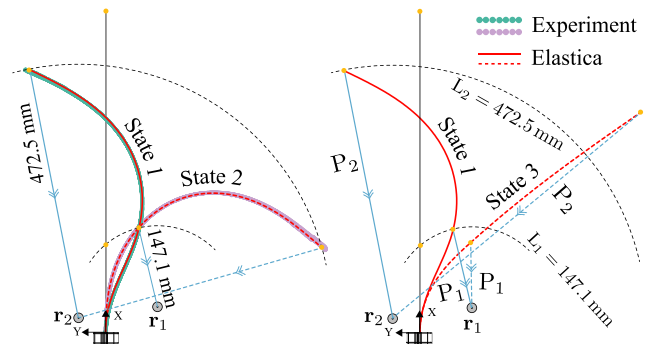
(a) Distinguishing configurations having identical cable lengths from configurations with identical cable tensions. States 1,2 and 3 are three equilibrium configurations of the arm in which states 1 and 2 are realized using the same pair of cable lengths, while states 1 and 3 are realized using the same pair of cable tensions. The image on the left also shows the shapes of experimental realizations of states 1 and 2 measured using a laser scanner.
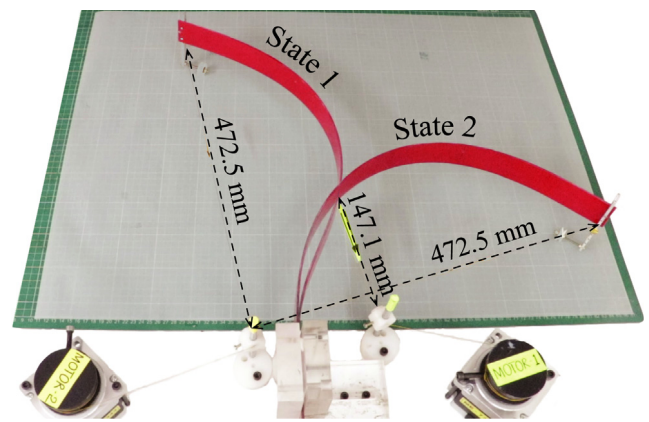

Fig. 8. An example demonstrating the possibility of solution multiplicity in load and length controlled settings. States 1 and 2 have identical cable lengths while states 1 and 3 have identical cable tensions.

tensions $(P_1 \ell^2/B, P_2 \ell^2/B) = (25.2, 10.8)$. In particular, neither of the cable lengths $(96.2, 454.3)$ mm in state 3 equal that of state 1, and neither of the cable tensions $(9.7, 12.6)$ in state 2 equal that of state 1.

Examining states 1 and 2 in Fig. 8 highlights an interesting feature. Starting from state 1, searching for an alternate equilibrium configuration satisfying the same tendon lengths requires the attachment point $\mathbf{x}_1$ to lie on a circle of radius $L_1 = 147.1$ mm centered at $\mathbf{r}_1$, and the tip $\mathbf{x}_2$ to lie on a circle of radius $L_2 = 472.5$ mm centered at $\mathbf{r}_2$. These circles are indicated by dashed lines in the figure. The two conditions impose severe kinematic constraints on state 2. For this reason, it is not possible to switch between states 1 to 2 using small or random perturbations. Instead, it is necessary to either add large perturbations to slacken both tendons and bias the arm towards the desired solution, or follow different loading sequences. Observe that the arm conveniently satisfies one of the two constraints in state 2, namely $L_1 = 147.1$ mm, by remaining unmoved from its location in state 1.

5. Concluding remarks

Using simple ideas from structural mechanics and optimization, we have demonstrated that it is possible to accurately position the tip of a flexible arm by manipulating it in non-intuitive

ways using a pair of tendons attached to its centerline. Compared to approaches prevalent in soft robotics, we exploit structural slenderness rather than a complex material response to achieve a high degree of controlled deformability. The resulting robot promises to be a useful device, besides adding to a growing list of applications based on the elastica model [16,33,35–37].

Our work suggests a number of directions for further investigation. The problem of a tendon-actuated elastica shows a diverse range of features (solution multiplicity, instabilities, configurational forces) and is an interesting system to study in its own right. Stability analysis of an elastica subject to cable length constraints appears to be a challenging problem, and may require techniques different from those used with load or displacement control [38]. Extensions of our work by combining tip control with shape control of the arm [26], permitting nonlinear material behavior, coupling actuation with energy recovery mechanisms, and generalization to the case of manipulating three-dimensional rods with general tendon routings will make the use of flexible elements more appealing in a wider range of applications. It is imperative to develop tools that will help to quantify workspaces of flexible robots [39]. Brute-force sampling techniques, such as the one we have used here, do not provide insights on the influence of various design parameters on the workspace. It also remains to be seen whether our approach can be extended to include dynamic effects.

Declaration of competing interest

The authors declare that they have no known competing financial interests or personal relationships that could have appeared to influence the work reported in this paper.

Acknowledgments

Appendix A. Supplementary data

Supplementary material related to this article can be found online at https://doi.org/10.1016/j.eml.2019.100584.

References

[1] J. Burgner-Kahrs, C. Rucker, H. Choset, Continuum robots for medical applications: A survey, IEEE Trans. Robot. 31 (6) (2015) 1261–1280.

[2] P. Polygerinos, Z. Wang, K. Galloway, R. Wood, C. Walsh, Soft robotic glove for combined assistance and at-home rehabilitation, Robot. Auton. Syst. 73 (2015) 135–143.

[3] S. Shian, K. Bertoldi, D. Clarke, Dielectric elastomer based grippers for soft robotics, Adv. Mater. 27 (43) (2015) 6814–6819.

[4] X. Zhou, C. Majidi, O. O'Reilly, Soft hands: An analysis of some gripping mechanisms in soft robot design, Int. J. Solids. Struct. 64 (2015) 155–165.

[5] W. Book, Controlled motion in an elastic world, J. Dyn. Syst. Meas. Control 115 (2B) (1993) 252–261.

[6] A. De Luca, W. Book, Robots with flexible elements, in: Springer Handbook of Robotics, Springer, Berlin, Heidelberg, 2008, pp. 287–319.

[7] D. Rus, M. Tolley, Design, fabrication and control of soft robots, Nature 521 (7553) (2015) 467.

[8] M. Tolley, R. Shepherd, B. Mosadegh, K. Galloway, M. Wehner, M. Karpelson, R. Wood, G. Whitesides, A resilient, untethered soft robot, Soft Robot. 1 (3) (2014) 213–223.

[9] C. Majidi, Soft robotics: a perspective, current trends and prospects for the future, Soft Robot. 1 (1) (2014) 5–11.

[10] D. Trivedi, C. Rahn, W. Kier, I. Walker, Soft robotics: Biological inspiration, state of the art, and future research, Appl. Bionics Biomech. 5 (3) (2008) 99–117.

[11] M. Benosman, G. Le Vey, Control of flexible manipulators: A survey, Robotica 22 (5) (2004) 533–545.

[12] M. Hannan, I. Walker, Kinematics and the implementation of an elephant's trunk manipulator and other continuum style robots, J. Robot. Syst. 20 (2) (2003) 45–63.

[13] G. Immega, K. Antonelli, The KSI tentacle manipulator, in: Proc. IEEE Int. Conf. Robot. Automat., Vol. 3, IEEE, 1995, pp. 3149–3154.

[14] W. McMahan, V. Chitrakaran, M. Csencsits, D. Dawson, I.D. Walker, B.A. Jones, M. Pritts, D. Dienno, M. Grissom, C.D. Rahn, Field trials and testing of the octarm continuum manipulator, in: Proc. IEEE Int. Conf. Robot. Autom., IEEE, 2006, pp. 2336–2341.

[15] C. Chou, B. Hannaford, Measurement and modeling of mckibben pneumatic artificial muscles, IEEE Trans. Robot. Autom. 12 (1) (1996) 90–102.

[16] K. de Payrebrune, O. O'Reilly, On constitutive relations for a rod-based model of a pneu-net bending actuator, Extreme Mech. Lett. 8 (2016) 38–46.

[17] F. Connolly, P. Polygerinos, C. Walsh, K. Bertoldi, Mechanical programming of soft actuators by varying fiber angle, Soft Robot. 2 (1) (2015) 26–32.

[18] F. Connolly, C. Walsh, K. Bertoldi, Automatic design of fiber-reinforced soft actuators for trajectory matching, Proc. Natl. Acad. Sci. 114 (1) (2017) 51–56.

[19] E. Bayo, A finite-element approach to control the end-point motion of a single-link flexible robot, J. Robot. Syst. 4 (1) (1987) 63–75.

[20] R. Cannon Jr, E. Schmitz, Initial experiments on the end-point control of a flexible one-link robot, Int. J. Robot. Res. 3 (3) (1984) 62–75.

[21] D. Wang, M. Vidyasagar, Transfer functions for a single flexible link, Int. J. Robot. Res. 10 (5) (1991) 540–549.

[22] R. Frisch-Fay, Flexible Bars, Butterworths, 1962.

[23] R. Webster III, B. Jones, Design and kinematic modeling of constant curvature continuum robots: A review, Int. J. Robot. Res. 29 (13) (2010) 1661–1683.

[24] C. Li, C. Rahn, Design of continuous backbone, cable-driven robots, J. Mech. Des. 124 (2) (2002) 265–271.

[25] C. Rucker, R. Webster III, Statics and dynamics of continuum robots with general tendon routing and external loading, IEEE Trans. Robot. 27 (6) (2011) 1033–1044.

[26] A. Nayak, P. Handral, R. Rangarajan, Shape control for the elastica through load optimization, J. Appl. Mech. 86 (1) (2019) 011011.

[27] L. Watson, C. Wang, A homotopy method applied to elastica problems, Int. J. Solids Struct. 17 (1) (1981) 29–37.

[28] M. Batista, Large deflection of cantilever rod pulled by cable, Appl. Math. Model. 39 (10–11) (2015) 3175–3182.

[29] J. Yau, Closed-form solutions of large deflection for a guyed cantilever column pulled by an inclination cable, J. Mar. Sci. Technol. 18 (1) (2010) 130–136.

[30] e.a. Satish Balay, PETSC web page, 2019, URL https://www.mcs.anl.gov/petsc.

[31] A. Kumar, T. Healey, A generalized computational approach to stability of static equilibria of nonlinearly elastic rods in the presence of constraints, Comput. Methods Appl. Mech. Engrg. 199 (25–28) (2010) 1805–1815.

[32] V. Hernandez, J. Roman, V. Vidal, SLEPC: A scalable and flexible toolkit for the solution of eigenvalue problems, ACM Trans. Math. Softw. 31 (3) (2005) 351–362.

[33] C. Armanini, F. Dal Corso, D. Misseroni, D. Bigoni, From the elastica compass to the elastica catapult: an essay on the mechanics of soft robot arm, Proc. R. Soc. Lond. Ser. A Math. Phys. Eng. Sci. 473 (2198) (2017) 20160870.

[34] J. Snyder, The elastica with end-load flip-over, J. Appl. Mech. 55 (1988) 845.

[35] F. Bosi, D. Misseroni, F. Dal Corso, D. Bigoni, An elastica arm scale, Proc. R. Soc. Lond. Ser. A Math. Phys. Eng. Sci. 470 (2169) (2014) 20140232.

[36] A. Cazzolli, D. Misseroni, F. Dal Corso, Elastica catastrophe machine: theory, design and experiments, J. Mech. Phys. Solids (2019) 103735.

[37] G. Cicconofri, A. DeSimone, A study of snake-like locomotion through the analysis of a flexible robot model, Proc. R. Soc. Lond. Ser. A Math. Phys. Eng. Sci. 471 (2184) (2015) 20150054.

[38] A. Cazzolli, F. Dal Corso, Snapping of elastic strips with controlled ends, Int. J. Solids Struct. 162 (2019) 285–303.

[39] T. Bretl, Z. McCarthy, Quasi-static manipulation of a Kirchhoff elastic rod based on a geometric analysis of equilibrium configurations, Int. J. Robot. Res. 33 (1) (2014) 48–68.